Effect of electromagnetic pulse transverse inhomogeneity on ion acceleration by radiation pressure

K. V. Lezhnin, F. F. Kamenets, V. S. Beskin, M. Kando, T. Zh. Esirkepov, and S. V. Bulanov

Citation: Physics of Plasmas (1994-present) **22**, 033112 (2015); doi: 10.1063/1.4915136
View online: http://dx.doi.org/10.1063/1.4915136
View Table of Contents: http://scitation.aip.org/content/aip/journal/pop/22/3?ver=pdfcov
Published by the AIP Publishing

Effect of electromagnetic pulse transverse inhomogeneity on ion acceleration by radiation pressure

K. V. Lezhnin,[1] F. F. Kamenets,[1] V. S. Beskin,[1,2] M. Kando,[3] T. Zh. Esirkepov,[3] and S. V. Bulanov[1,3,a)]

[1]*Moscow Institute of Physics and Technology, Institutskiy per. 9, Dolgoprudny, Moscow Region 141700, Russia*

[2]*P. N. Lebedev Physics Institute of Russian Academy of Sciences, Leninskii Prosp 53, Moscow 119991, Russia*

[3]*Japan Atomic Energy Agency, Kansai Photon Science Institute, 8-1-7 Umemidai, Kizugawa-shi, Kyoto 619-0215 Japan*

(Received 25 December 2014; accepted 5 March 2015; published online 19 March 2015)

During ion acceleration by radiation pressure, a transverse inhomogeneity of an electromagnetic pulse leads to an off-axis displacement of the irradiated target, limiting the achievable ion energy. This effect is analytically described within the framework of a thin foil target model and with particle-in-cell simulations showing that the maximum energy of the accelerated ions decreases as the displacement from the axis of the target's initial position increases. The results obtained can be applied to the optimization of ion acceleration by the laser radiation pressure with mass-limited targets. © *2015 AIP Publishing LLC*. [http://dx.doi.org/10.1063/1.4915136]

I. INTRODUCTION

Studies of the high-energy ion generation in the interaction between an ultra-intense laser pulse and a small overdense target are of fundamental importance for various research fields, ranging from the development of ion sources for thermonuclear fusion and medical applications to the investigation of high energy density phenomena in relativistic astrophysics (see review articles[1–7] and the literature cited therein).

Theory and experiments on laser acceleration can clarify the basic features of particle acceleration in astrophysical objects. Indeed, according to the common viewpoint, activities of radio pulsars, active galactic nuclei, and even gamma-bursters are related to a highly magnetized wind wherein the electric field strength is approximately equal to the magnetic one.[8] Charged particles produced in such a wind can acquire energies of the order of $m_\alpha c^2 \gamma_w^2$, which is much higher than the energy of the wind ($\approx mc^2\gamma_w$).[9,10] Here, γ_w is the Lorentz-factor associated with the wind velocity. Moreover, regions where the electric field is stronger than the magnetic field can form in the interaction of the wind with external environments, such as a companion star in a close binary system or current sheets in pulsar winds. In these regions, the acceleration of particles can be even more effective.[11,12]

Depending on the laser and target parameters, different regimes of ion acceleration can occur, such as acceleration at the target surface, known as the target normal sheath acceleration (TNSA),[13–16] Coulomb explosion,[17–20] and the radiation pressure-dominant acceleration (RPDA) regime.[21–24] These regimes are shown on the plane of the laser intensity and the target surface density $n_e l_0$ in Fig. 1 (see also Ref. 6). Here, n_e and l_0 are the electron density and thickness of the target, respectively. At the intensities above $10^{18}\mathrm{W/cm}^2$, the plasma electron energy becomes relativistic. In Fig. 1, the dashed line is given by the formula

$$a_0 = n_e r_e \lambda l_0, \tag{1}$$

where $a_0 = eE_0/m_e\omega c$ is the dimensionless laser pulse amplitude, ω and $\lambda = 2\pi c/\omega$ are the laser frequency and wavelength, respectively, and $r_e = e^2/m_e c^2 = 2.8 \times 10^{-13}$ cm is the classical electron radius, where m_e and e are the electron mass and charge, respectively, and c is the speed of light in vacuum. This line separates the intensity–surface density plane into two domains. Below the line, plasma is opaque to laser radiation; above the line, plasma is transparent.[25,26] When the laser radiation interacts with an opaque target, a relatively small portion of hot electrons can escape, forming a sheath with a strong electric charge separation. The corresponding electric field accelerates ions in the TNSA regime. Above the dashed line, the laser radiation is so intense that it blows out almost all electrons from the irradiated region of the target. The remaining ions undergo fast expansion, known as Coulomb explosion, due to the repelling of noncompensated electric charges. At the opaqueness–transparency threshold, in the vicinity of the dashed line in Fig. 1, the optimal conditions for ion acceleration in the RPDA regime are realized.[22,27,28] A fundamental feature of the RPDA acceleration process noticed by Veksler[21] is high efficiency: in the ultrarelativistic limit, the ion energy per nucleon turns out to be proportional to the electromagnetic pulse energy. As far as it concerns the experimental evidence of the RPDA mechanism, there are indications of its realization in the laser–thin foil interactions reported in Refs. 29–31.

In investigations of laser-driven ion acceleration, considerable attention is paid to a target with a small transverse size, comparable with the laser pulse waist. Such a target is called a mass limited target (MLT) or reduced mass

[a)]Also at the ITMO University, Saint-Petersburg 197101, Russia; A. M. Prokhorov General Physics Institute of Russian Academy of Sciences, Vavilov Str. 38, Moscow 119991, Russia

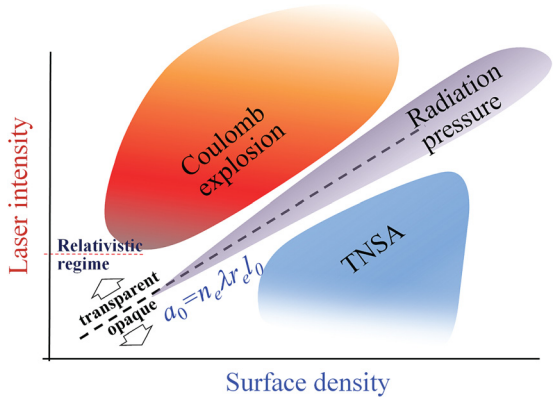

FIG. 1. The ion acceleration regimes in the plane of the laser intensity I and the surface density of the target $n_e l_0$. The dashed line is described by Eq. (1).

target;[32–38] this concept also includes cluster targets.[18,39] The use of MLT enables the enhancement of the ion energy and acceleration efficiency, and provides an opportunity for high-brightness X-ray generation.[40,41] The irradiation of an MLT by enough high intensity lasers is one of the most promising approaches to the development of compact ion accelerators.[42,43] We also note that in the RPDA regime of laser-foil interaction,[22–24] the accelerated high-density portion of plasma tears off the foil and becomes an MLT; hence, the interaction with the MLT is a generic case of the RPDA regime.

In this study, we discuss the RPDA regime when a transversely inhomogeneous laser pulse irradiates an MLT positioned slightly off the laser pulse axis. This situation naturally occurs due to the limited pointing stability of a laser system. As a result, the transverse component of the radiation pressure leads to the displacement of the irradiated target in the off-axis direction. Apparently, after a finite time interval, the target moves out of the laser pulse, so that the ion acceleration ceases. Below, using a theoretical model of a relativistic mirror,[22,40,42,43] we calculate the acceleration time and the achieved ion energy depending on the laser pulse amplitude and waist, and the initial displacement of the target from the laser axis. According to recent studies, various instabilities of the target plasma appear in the RPDA regime. For instance, a Rayleigh–Taylor-like instability[44,45] leads to the target modulation forming low-density bubbles and high-density clumps, resulting in a broadening of the accelerated ion energy spectrum. To elucidate the kinetic and nonlinear effects and instabilities, we conduct the particle-in-cell (PIC) simulations of the finite waist laser pulse interaction with the MLT using the REMP code.[46]

II. THE DYNAMICS OF A MASS–LIMITED TARGET POSITIONED SLIGHTLY OFF-AXIS

A. The equations of motion

We describe the nonlinear dynamics of a laser accelerated target within the framework of the thin shell approximation formulated by Ott[47] and further generalized to the 3D geometry in Refs. 48 and 49 and extended to the relativistic case in Refs. 42–45.

Following Refs. 42–45, here we derive a model for the MLT dynamics. The equations of motion of the surface element of a thin foil target in the laboratory frame of reference can be written in the form

$$\frac{d\mathbf{p}}{dt} = \frac{\mathcal{P}\nu}{\sigma}, \tag{2}$$

where $\mathbf{p}$, $\mathcal{P}$, ν, and σ are the momentum, light pressure, unit vector normal to the target surface element, and surface density, $\sigma = nl_0$, respectively. Here, n and l are the plasma ion density and target thickness, respectively. The surface element Δs carries $\Delta N = \sigma \Delta s$ particles, where ΔN is a constant in time. We assume that the target is initially at rest, at $t = 0$, in the plane $x = 0$. To describe how its shape and position change with time, it is convenient to introduce the Lagrange coordinates, η and ζ, playing the roles of the markers of a target surface element. The target surface shape and position are represented by the following function:

$$\mathbf{M} = \mathbf{M}(\eta, \zeta, t) \equiv \{x(\eta, \zeta, t), y(\eta, \zeta, t), z(\eta, \zeta, t)\}. \tag{3}$$

At a regular point, the surface area of a target element and the unit vector normal to the target are equal to

$$\nu \Delta s = \partial_\eta \mathbf{M} \times \partial_\zeta \mathbf{M}\, \mathrm{d}\eta \mathrm{d}\zeta \tag{4}$$

and

$$\nu = \frac{\partial_\eta \mathbf{M} \times \partial_\zeta \mathbf{M}}{|\partial_\eta \mathbf{M} \times \partial_\zeta \mathbf{M}|}, \tag{5}$$

respectively (see, e.g., Ref. 50). The conservation of particle number implies that $\sigma \Delta s = \sigma_0 \Delta s_0$, where $\sigma_0 = n_0 l_0$. This yields

$$\sigma = \frac{\sigma_0}{|\partial_\eta \mathbf{M} \times \partial_\zeta \mathbf{M}|}. \tag{6}$$

Using these relationships and representing the coordinates x_i as

$$x = \xi_x(\eta, \zeta, t), \tag{7}$$

$$y = \eta + \xi_y(\eta, \zeta, t), \tag{8}$$

$$z = \zeta + \xi_z(\eta, \zeta, t) \tag{9}$$

with initial conditions $\xi_i(\eta, \zeta, 0) = 0$ and $\dot{\xi}_i(\eta, \zeta, 0) = v_i(\eta, \zeta, 0)$, we obtain the equations of motion in the form[45]

$$\sigma_0 \partial_t p_x = \mathcal{P}(1 + \partial_\eta \xi_y + \partial_\zeta \xi_z + \{\xi_y, \xi_z\}), \tag{10}$$

$$\sigma_0 \partial_t p_y = \mathcal{P}(-\partial_\eta \xi_x + \{\xi_z, \xi_x\}), \tag{11}$$

$$\sigma_0 \partial_t p_z = \mathcal{P}(-\partial_\zeta \xi_x + \{\xi_x, \xi_y\}), \tag{12}$$

$$\partial_t \xi_i = c \frac{p_i}{\left(m_\alpha^2 c^2 + p_k p_k\right)^{1/2}}, \tag{13}$$

Here, m_α is the ion mass; $i = 1$, 2, and 3; repeated indices implicitly denote summation; and

$$\{\xi_j, \xi_k\} = \partial_\eta \xi_j \partial_\zeta \xi_k - \partial_\zeta \xi_j \partial_\eta \xi_k \tag{14}$$

are Poisson's brackets. This form of these equations is particularly convenient for analyzing a small but finite displacement of the target element from the axis.

The radiation pressure exerted on the target by a circularly polarized electromagnetic wave propagating along the x-axis with amplitude $E = E(t - x/c)$ is

$$\mathcal{P} = K\frac{E^2}{4\pi}\left(\frac{1-\beta_x}{1+\beta_x}\right), \tag{15}$$

where $\beta_x = p_x(m_\alpha^2 c^2 + p_x^2)^{-1/2}$ is the target element normalized velocity in the x-direction. The coefficient K is equal to

$$K = 2|\rho|^2 + |\alpha|^2, \tag{16}$$

where $|\rho|^2$ and $|\alpha|^2$ are the light reflection and absorption coefficients, respectively (see also Refs. 51 and 52). The effects of the reflection coefficient dependence on the ion energy due to the relativistic transparency have been discussed in Refs. 27 and 28. For simplicity, we assume an ideally reflective target with $K = 2$.

We note here that in Eqs. (10)–(12), there is no interaction between the target surface elements. We consider a MLT for which the Lagrange coordinates η and ζ belong to a finite domain, $\eta \in [\eta_1, \eta_2]$ and $\zeta \in [\zeta_1, \zeta_2]$.

For a homogeneous laser pulse, $E =$ constant, the flat MLT is accelerated along the x-axis with $p_y = 0$, $p_z = 0$, $\xi_y = 0$, and $\xi_z = 0$. The ion momentum and displacement in the x-direction depend on time in the following way:[22]

$$p_x^{(0)}(t) = m_\alpha c\left(\frac{t}{t_{1/3}}\right)^{1/3}, \tag{17}$$

$$\xi_x^{(0)}(t) = ct - 3ct_{1/3}^{2/3}t^{1/3}, \tag{18}$$

where the characteristic time is

$$t_{1/3} = \frac{8\pi\sigma_0 m_\alpha c}{3E^2}. \tag{19}$$

Here, we assume that the target energy is ultrarelativistic, $p_x^{(0)}/m_\alpha c \gg 1$.

Using relationships (17) and (18), we can easily find that the finite-duration laser pulse, t_{las}, accelerates the ions up to energy $\mathcal{E} = m_\alpha c^2 \gamma_{max}$ with the gamma-factor given by

$$\gamma_{max} = \frac{E^2 t_{las}}{4\pi\sigma_0 m_\alpha c}. \tag{20}$$

According to Eq. (17), the acceleration time, t_{acc}, can be defined via $\gamma_{max} = (t_{acc}/t_{1/3})^{1/3}$, assuming that at the end of acceleration the laser pulse rear reaches the target, as it is illustrated in Fig. 2. Thus, the acceleration time is determined by equation

$$t_{las} = \int_0^{t_{acc}}\left(1 - \frac{v(t)}{c}\right)dt \approx \frac{1}{2}\int_0^{t_{acc}}\frac{dt}{\gamma(t)^2}dt. \tag{21}$$

Equations (20) and (21) yield

$$t_{acc} = \frac{2}{3}\gamma_{max}^2 t_{las}. \tag{22}$$

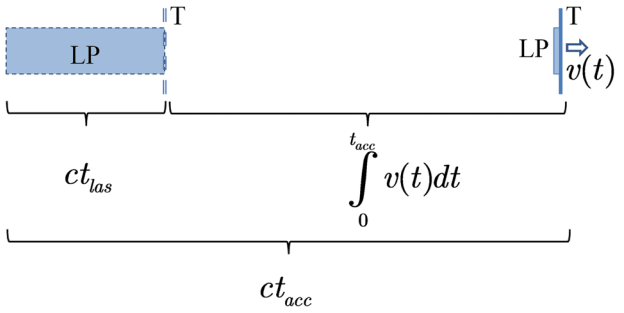

FIG. 2. The relative positions of the laser pulse (LP), having a duration of t_{las}, and the target (T), acquiring the velocity of $v(t)$, at the beginning of the interaction, $t = 0$, and at the time when the laser pulse rear reaches the target, $t = t_{acc}$.

B. Mass limited target irradiated by a Gaussian laser pulse

In order to analyze the transverse motion of the MLT irradiated by the laser pulse, we consider the pulse with an envelope of Gaussian form

$$E(y,z) = E_0 \exp\left(-\frac{y^2}{2l_y^2} - \frac{z^2}{2l_z^2}\right), \tag{23}$$

where the laser pulse width equals l_y and l_z in the y- and z-directions, respectively.

Assuming a small transverse displacement, $\xi_y \ll \eta$, $\xi_z \ll \zeta$, and considering the near-axis region, $\eta \ll l_y$, $\zeta \ll l_z$, we obtain the linearized system of equations from Eqs. (10)–(12):

$$\partial_t\left(\left(\gamma^{(0)}(t)\right)^3 \partial_t \xi_x^{(1)}\right) = \frac{c}{\left(\gamma^{(0)}(t)\right)^2 t_{1/3}^{(0)}} \times \left(\partial_\eta \xi_y^{(1)} + \partial_\zeta \xi_z^{(1)} - \frac{\eta^2}{l_y^2} - \frac{\zeta^2}{l_z^2}\right), \tag{24}$$

$$\partial_t\left(\gamma^{(0)}(t)\partial_t \xi_y^{(1)}\right) = -\frac{c}{\left(\gamma^{(0)}(t)\right)^2 t_{1/3}^{(0)}}\partial_\eta \xi_x^{(1)}, \tag{25}$$

$$\partial_t\left(\gamma^{(0)}(t)\partial_t \xi_z^{(1)}\right) = -\frac{c}{\left(\gamma^{(0)}(t)\right)^2 t_{1/3}^{(0)}}\partial_\zeta \xi_x^{(1)} \tag{26}$$

with a given dependence on time of the ion gamma-factor

$$\gamma^{(0)}(t) = \left(\frac{t}{t_{1/3}^{(0)}}\right)^{1/3}, \tag{27}$$

which is found within the framework of the 1D model of thin foil RPDA.[22] This approach corresponds to a so-called betatron approximation, which is well known in the theory of standard accelerators of charged particles.[53] In these expressions, the characteristic time is $t_{1/3}^{(0)} = 8\pi\sigma_0 m_\alpha c/3E_0^2$.

To find the solution to the system of partial differential equations, Eqs. (24)–(26), we use the ansatz

$$\xi_x^{(1)}(\eta,\zeta,t) = \Xi_x(t) + \Xi_{x\eta\eta}(t)\eta^2 + \Xi_{x\zeta\zeta}(t)\zeta^2, \tag{28}$$

$$\xi_y^{(1)}(\eta,\zeta,t) = \Xi_{y\eta}(t)\eta, \tag{29}$$

$$\xi_z^{(1)}(\eta,\zeta,t) = \Xi_{z\zeta}(t)\zeta, \tag{30}$$

which is a self-similar solution reducing Eqs. (24)–(26) to ordinary differential equations for the functions $\Xi_x(t)$, $\Xi_{x\eta\eta}(t)$, $\Xi_{x\zeta\zeta}(t)$, $\Xi_{y\eta}(t)$, and $\Xi_{z\zeta}(t)$:

$$\frac{d}{d\tau}\left(\gamma^{(0)}\frac{d\,\Xi_{x\eta\eta}}{d\tau}\right) = -\frac{1}{l_y^2}, \tag{31}$$

$$\frac{d}{d\tau}\left(\gamma^{(0)}\frac{d\,\Xi_{x\zeta\zeta}}{d\tau}\right) = -\frac{1}{l_z^2}, \tag{32}$$

$$\frac{d}{d\tau}\left(\frac{1}{\gamma^{(0)}}\frac{d\,\Xi_{y\eta}}{d\tau}\right) = -2\Xi_{x\eta\eta}, \tag{33}$$

$$\frac{d}{d\tau}\left(\frac{1}{\gamma^{(0)}}\frac{d\,\Xi_{z\zeta}}{d\tau}\right) = -2\Xi_{x\zeta\zeta}, \tag{34}$$

$$\frac{d}{d\tau}\left(\gamma^{(0)}\frac{d\,\Xi_x}{d\tau}\right) = \Xi_{y\zeta} + \Xi_{z\zeta}. \tag{35}$$

We introduced a new independent variable equal to

$$\tau = \left(\frac{c}{t_{1/3}^{(0)}}\right)^{1/2}\int_0^t \frac{dt}{\left(\gamma^{(0)}(t)\right)^2} \approx 3c^{1/2}\left(t_{1/3}^{(0)}\right)^{1/6} t^{1/3}. \tag{36}$$

For the initial conditions $\xi_x^{(1)}(\eta,\zeta,0) = 0$ and $\dot{\xi}_x^{(1)}(\eta,\zeta,0) = 0$, the solution to Eqs. (31)–(35) reads

$$\Xi_{x\eta\eta} = -\frac{9ct}{l_y^2}\left(\frac{t_{1/3}}{t}\right)^{2/3},\ \Xi_{x\zeta\zeta} = -\frac{9ct}{l_z^2}\left(\frac{t_{1/3}}{t}\right)^{2/3}, \tag{37}$$

$$\Xi_{y\eta} = \frac{81(ct)^2}{4\,l_y^2}\left(\frac{t_{1/3}}{t}\right)^{2/3},\ \Xi_{z\zeta} = \frac{81(ct)^2}{4\,l_z^2}\left(\frac{t_{1/3}}{t}\right)^{2/3}, \tag{38}$$

$$\Xi_x = -\frac{729(ct)^3}{100}\left(\frac{t_{1/3}}{t}\right)^{4/3}\left(\frac{1}{l_y^2}+\frac{1}{l_z^2}\right). \tag{39}$$

As seen from Eqs. (29) and (38), the target element with initial coordinates η and ζ moves in the transverse direction with a displacement proportional to $t^{4/3}$. We can estimate the time required to leave the region with a strong laser field as follows:

$$\delta t_\perp = \left(\frac{4l_\perp^3}{81\delta r_0}\right)^{3/4}\frac{1}{c^{3/2}t_{1/3}^{1/2}}, \tag{40}$$

where $l_\perp = \min\{l_y, l_z\}$ and $\delta r_0 = \max\{\eta,\zeta\}$. According to Eqs. (20) and (40), the achieved ion energy is of the order of

$$\mathcal{E}_\alpha = m_\alpha c^2\left(\frac{\delta t_\perp}{t_{1/3}}\right)^{1/3}, \tag{41}$$

which implies that $\delta t_\perp < t_{acc}$. The opposite case is realized for a small enough initial position of the MLT centroid, δr_0, and/or a wide enough laser pulse, which corresponds to a perfect laser-target alignment.

Using the relationships obtained above, we can write the characteristic time $t_{1/3}$ as follows:

$$t_{1/3} = \frac{2\omega_{pe}^2}{\omega^2}\frac{m_\alpha}{m_e}\frac{l_0}{c}\frac{1}{a_0^2}. \tag{42}$$

For a solid density target, $\omega_{pe}^2/\omega^2 \approx 10^2$, with a thickness of $l_0 = 0.1\mu$ m, and for a laser intensity of the order of 10^{23} W/cm^2 (corresponding to $a_0 = 300$), protons ($m_\alpha = m_p$) are accelerated with a characteristic time of $t_{1/3} \approx 1.5$ fs. In the case of the perfect laser-target alignment, the maximum achievable ion (proton) energy is $m_\alpha c^2(t_{las}/3t_{1/3})$. For a 100 fs laser pulse duration, it is about 20 GeV with an acceleration time of 10 ps, as given by Eq. (22). The perfect alignment condition implies that $\delta t_\perp > t_{acc}$.

C. Super-Gaussian laser pulse interaction with a mass limited target

Here, we analyze the case wherein the laser pulse envelope has a super-Gaussian form

$$E(y,z) = E_0\exp\left(-\frac{y^4}{2l_y^4}\right) \tag{43}$$

with the index equal to 4. For the sake of brevity, we consider 2D geometry. Generalization to the 3D case is then straightforward.

For a small transverse displacement, $\xi_y \ll \eta$, in the near-axis region, $\eta \ll l_y$, within the framework of the betatron approximation, the target dynamics are described by the following linearized system of equations:

$$\partial_\tau\left(\gamma^{(0)}\partial_\tau\xi_x^{(1)}\right) = \partial_\eta\xi_y^{(1)} - \frac{\eta^4}{l_y^4}, \tag{44}$$

$$\partial_\tau\left(\frac{1}{\gamma^{(0)}}\partial_\tau\xi_y^{(1)}\right) = \partial_\eta\xi_x^{(1)} \tag{45}$$

with the independent variable τ defined by Eq. (36) and the ion gamma-factor $\gamma^{(0)}$ given by Eq. (27).

The self-similar solution to Eqs. (44) and (45) has the following form:

$$\xi_x^{(1)}(\eta,\tau) = \Xi_x(\tau) + \Xi_{x\eta\eta}(\tau)\eta^2 + \Xi_{x\eta\eta\eta\eta}(\tau)\eta^4, \tag{46}$$

$$\xi_y^{(1)}(\eta,\tau) = \Xi_{y\eta}(\tau)\eta + \Xi_{y\eta\eta\eta}(\tau)\eta^3. \tag{47}$$

Substituting these functions into Eqs. (44) and (45), we obtain the following ordinary differential equations:

$$\frac{d}{d\tau}\left(\gamma^{(0)}\frac{d\,\Xi_{x\eta\eta\eta\eta}}{d\tau}\right) = -\frac{1}{l_y^4}, \tag{48}$$

$$\frac{d}{d\tau}\left(\frac{1}{\gamma^{(0)}}\frac{d\,\Xi_{y\eta\eta\eta}}{d\tau}\right) = -4\,\Xi_{x\eta\eta\eta\eta}, \tag{49}$$

$$\frac{d}{d\tau}\left(\gamma^{(0)}\frac{d\,\Xi_{x\eta\eta}}{d\tau}\right) = 3\,\Xi_{y\eta\eta\eta}, \tag{50}$$

$$\frac{d}{d\tau}\left(\frac{1}{\gamma^{(0)}}\frac{d\,\Xi_{y\eta}}{d\tau}\right) = -2\,\Xi_{x\eta\eta}, \tag{51}$$

$$\frac{d}{d\tau}\left(\gamma^{(0)}\frac{d\,\Xi_{x}}{d\tau}\right) = \Xi_{y\eta}. \tag{52}$$

For the initial displacement $\xi_i^{(1)}(\eta,0)=0$ and its time derivative $\dot{\xi}_i^{(1)}(\eta,0)=0$, the solution to Eqs. (48)–(52) is

$$\Xi_{x\eta\eta\eta} = -\frac{9ct}{l_y^4}\left(\frac{t_{1/3}}{t}\right)^{2/3}, \quad \Xi_{y\eta\eta\eta} = \frac{81(ct)^2}{2\,l_y^4}\left(\frac{t_{1/3}}{t}\right)^{2/3}, \tag{53}$$

$$\Xi_{x\eta\eta} = \frac{4374(ct)^3}{100\,l_y^4}\left(\frac{t_{1/3}}{t}\right)^{4/3}, \quad \Xi_{y\eta} = -\frac{6561(ct)^4}{400\,l_y^4}\left(\frac{t_{1/3}}{t}\right)^{4/3}, \tag{54}$$

$$\Xi_{x} = -\frac{285768(ct)^5}{156800\,l_y^4}\left(\frac{t_{1/3}}{t}\right)^{2}. \tag{55}$$

As seen from expressions (44) and (45) and (53)–(55), the target is deformed in such a way that its periphery expands and its near-axis region contracts. This somewhat paradoxical behavior can be explained as follows. Due to the decrease in the density, the target elements move forward faster on the periphery than in the near-axis region. Therefore, the target curvature changes, resulting in the contraction of the near-axis elements, which is distinctly seen in Fig. 3. The longitudinal velocity (along the x-axis) has two maxima. The transverse velocity gradient (along the y-axis) is positive at large y and negative near the axis, which corresponds, respectively, to the foil expansion on the periphery and to the foil compression near the axis.

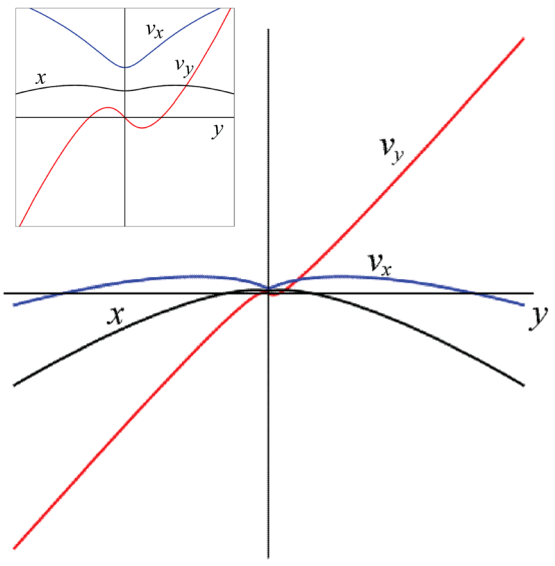

FIG. 3. The deformation of a thin target accelerated by a super-Gaussian laser pulse according to Eqs. (44), (45), and (53)–(55), for $l_y/ct_{1/3}=2$ at $t/t_{1/3}=0.5$. The curves x, v_x, and v_y that are the target position along the x-axis, and the x- and y-components of the target element velocity, respectively, are shown in the (y, x) plane (here, y-axis is horizontal, x-axis is vertical). Inset: the near-axis region magnified.

III. THE RESULTS OF PARTICLE-IN-CELL SIMULATIONS

Theoretical analysis of the target off-axis displacement effects is conducted above within the framework of the linearized model equations (24)–(26). To consider the nonlinear and kinetic effects, as well as the target deformation and instability, we have conducted a series of 2D PIC simulations using the relativistic electromagnetic code REMP.[46]

The simulation box is $300\lambda \times 100\lambda$ with a mesh resolution of 20 cells per laser wavelength λ. The total number of quasi-particles is equal to 7×10^4. The target has the form of an ellipsoid in the (x, y) plane, with horizontal and vertical semi-axes equal to 1λ and 3.5λ, respectively. It is initially located at $x=50\lambda$ in the near-axis region. The initial transverse shift of the target (along the y-axis) varies from 0 to 1.8λ. The target comprises hydrogen plasma with a proton-to-electron mass ratio of 1836. The electron density corresponds to the ratio $\omega_{pe}/\omega=10$. A circularly polarized laser pulse is excited in the vacuum region at the left-hand side of the computation domain. The laser pulse has a Gaussian shape with a length of $l_x=20\lambda$ and $l_y=25\lambda$, and its dimensionless amplitude $a=eE/m_e\omega c$ varies from 250 to 325. Under the simulation conditions, the accelerated ion energy according to Eq. (20) is equal to 4.5 GeV. The acceleration length $l_{acc}=ct_{acc}$ is equal to 135λ.

The chosen laser amplitude a is close to the threshold above which it is necessary to consider the radiation reaction effects on the level of individual electrons[54,55]

$$a_{RR} = \left(\frac{3\lambda_M}{4\pi r_e}\right)^{1/3}, \tag{56}$$

where λ_M is the radiation wavelength in the frame of reference comoving with the accelerated target, ($\lambda_M \approx 2\gamma\lambda_0$). For $\lambda_0=1\mu m$ and a relativistic gamma factor corresponding to the accelerated ion energy of the order of 8 GeV (see below), the threshold amplitude is $a_{RR}=915$. This corresponds to an intensity of $I\approx10^{24}$ W/cm^2, which is substantially larger than that in our simulations. Tamburini *et al.*[56] have found that at an intensity of $I\approx10^{23}$ W/cm^2, close to the parameters of our simulations, the radiation reaction effects, although noticeable, do not drastically modify the ion acceleration process. Here, we note that in the range of parameters under consideration, quantum electrodynamics effects can weaken the radiation reaction force.[7,57,58]

The aim of PIC simulations is to investigate the dependence of the energy of accelerated ions on the initial displacement of the target along the y-axis.

In Figs. 4(a)–4(d), we present the electromagnetic field and electron and ion density distributions in the (x, y) plane at $t=100$. Here, and below, the laser's period $2\pi/\omega$ and wavelength λ are the time and space units, respectively. Fig. 4(b), with the distribution of the z-component of the electromagnetic field in the (x, y) plane, shows the laser pulse reflection from the target receding with relativistic velocity. Due to the double Doppler effect, the wavelength of the reflected light is substantially longer than that of the incident radiation. The laser field interaction with the plasma target is

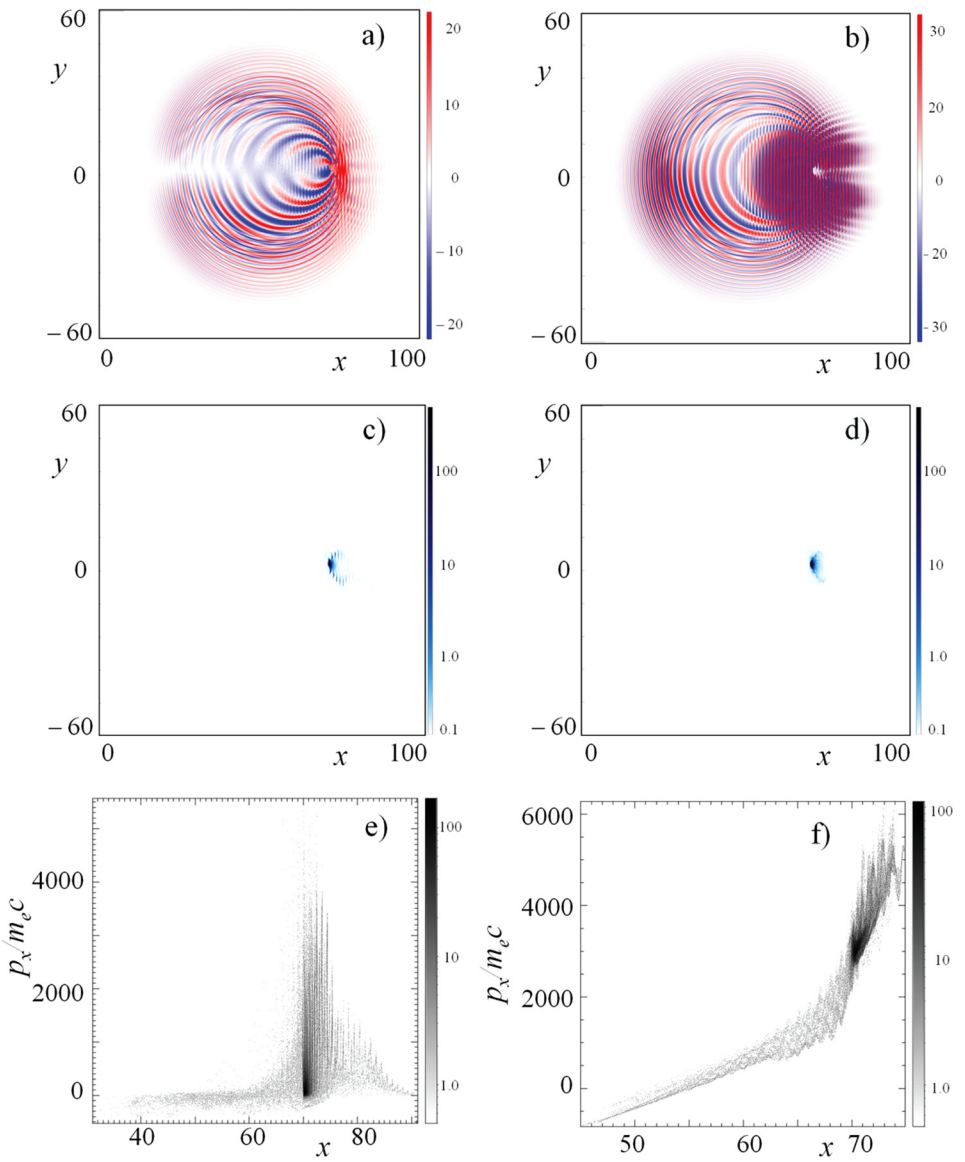

FIG. 4. The distributions of (a) the x- and (b) z-components of the electric field and (c) the electron and (d) ion density in the (x, y) plane. The phase planes (x, p_x) of (e) the electrons and (f) the ions. All the frames are taken for $t = 100$. The initial off-axis displacement of the target is $\delta y = 0.25\lambda$.

accompanied by a high-order harmonics generation that is distinctly seen as the short-wavelength scattered radiation. The up–down asymmetry of the $E_x(x, y)$ component appears due to the asymmetry of the initial position of the target with respect to the laser pulse axis. One can also see a strong longitudinal quasistatic (long–wavelength) electric field formed at the rear side of the target. This field is due to the electric charge separation and it accelerates positively charged ions. From Figs. 4(c) and 4(d), it follows that where the electron and ion density distributions in the (x, y) plane are shown, the electrons pushed forward by the laser radiation almost move together with the ions pulled by the electric field. In Figs. 4(e) and 4(f), we present the phase planes (x, p_x) of the electrons and ions, respectively, which demonstrate that the electrons and ions with the highest energy are localized in the same region.

In the process of nonlinear interaction with the MLT, the laser pulse becomes modulated in the transverse direction, as is seen in Fig. 4(b). This makes the interaction with the target of initially Gaussian pulse to be similar to that of the super-Gaussian pulse. As a result, the dependences of the x- and y-components of the ion and electron momentum on the y-coordinate shown in Fig. 5 are in qualitative agreement with theoretical curves in Fig. 3. Here, it is possible to see a characteristic double maximum profile in the ion distribution in the (y, p_x) plane. The (y, p_y) distribution clearly shows the target expansion on the periphery and the contraction in the near-axis region.

In Figs. 6(a) and 6(b), where we plot the distributions of the electron and ion density in the (x, y) plane at $t = 250$, we see that the ions and electrons are mostly localized in the same region, although the target is strongly deformed and displaced in the vertical direction. Figs. 6(c) and 6(d) present the phase planes (x, p_x) of the electrons and ions, with insets showing the electron and ion energy spectra, respectively. The electron component has a flat energy distribution with a maximum energy of the order of 8 GeV. The accelerated ion energy distribution shows a relatively narrow, approximately 20%, peak at an energy of the order of 4 GeV. The ion phase planes (y, p_x) and (y, p_y) in Figs. 6(e) and 6(f) demonstrate that high-energy ions remain localized in the near-axis region.

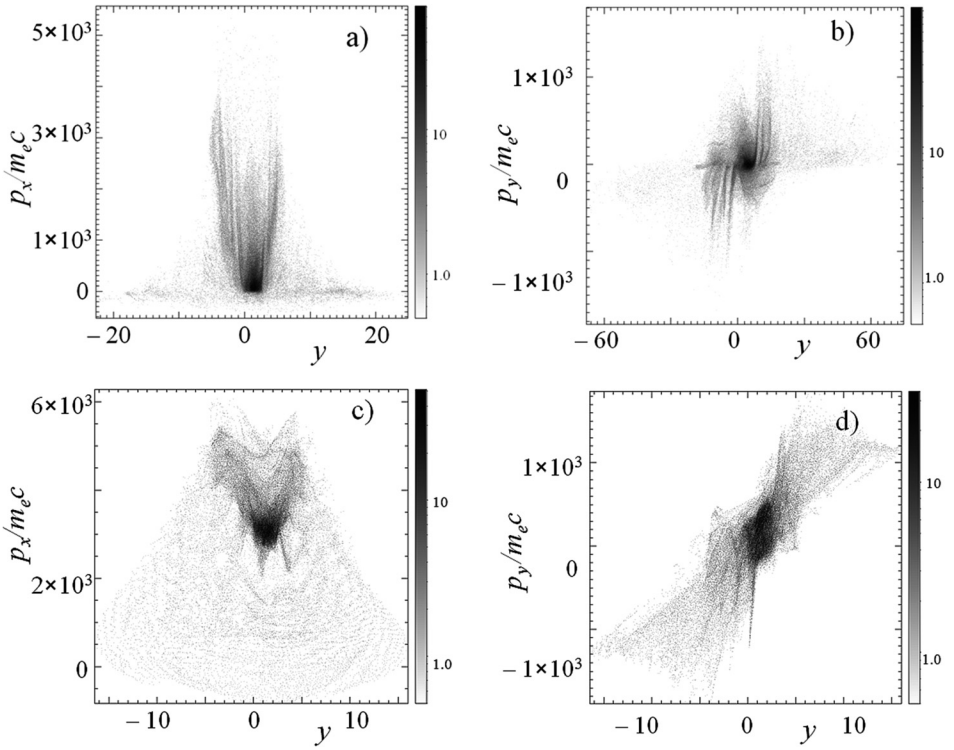

FIG. 5. The phase planes (y, p_x) and (y, p_y) for electrons (a) and (b), and for ions (c) and (d), respectively, at $t = 100$. The initial off-axis displacement of the target is $\delta y = 0.25\lambda$.

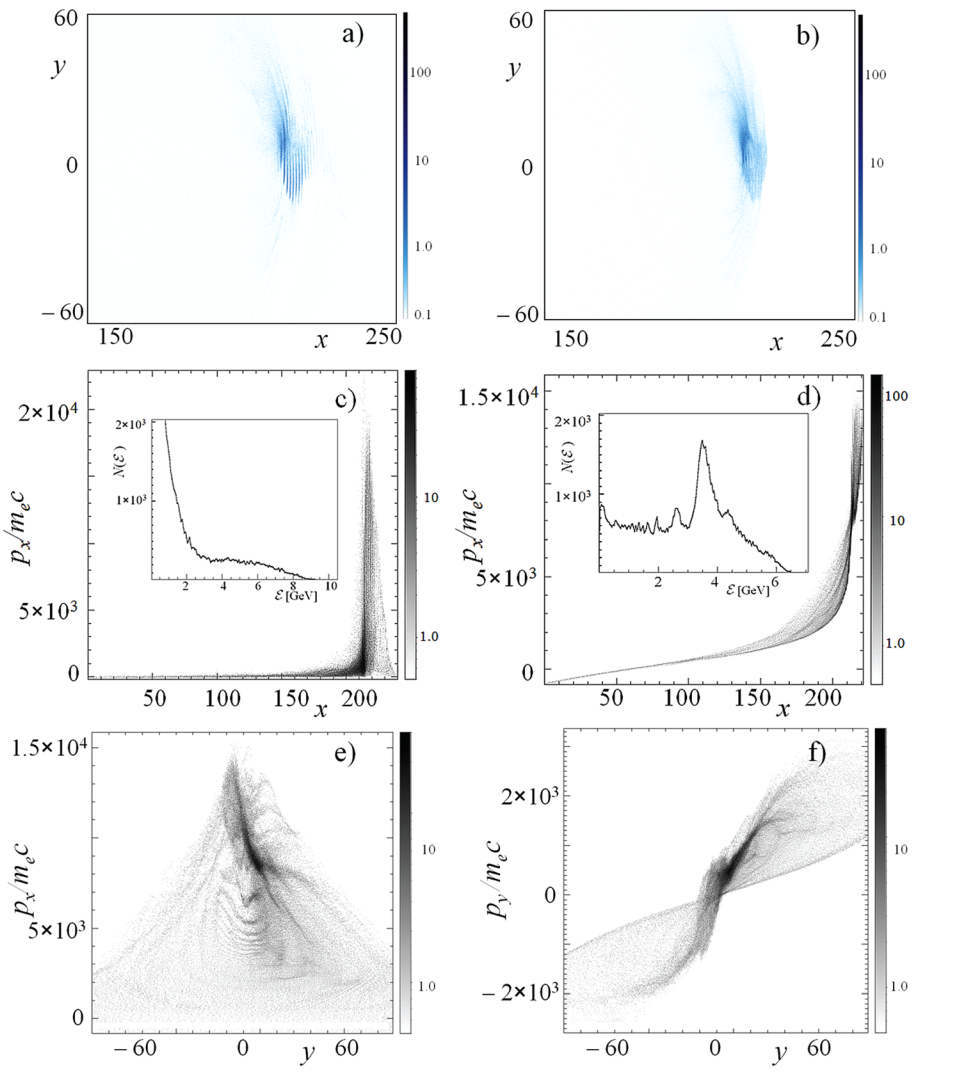

FIG. 6. The distributions of (a) the electron and (b) ion density in the (x, y) plane. (c) and (d) The phase plane (x, p_x) and the energy spectrum (inset) of (c) the electrons and (d) ions. The ion phase planes (e) (y, p_x) and (f) (y, p_y). All the frames for $t = 250$. The initial off-axis displacement of the target is $\delta y = 0.25\lambda$.

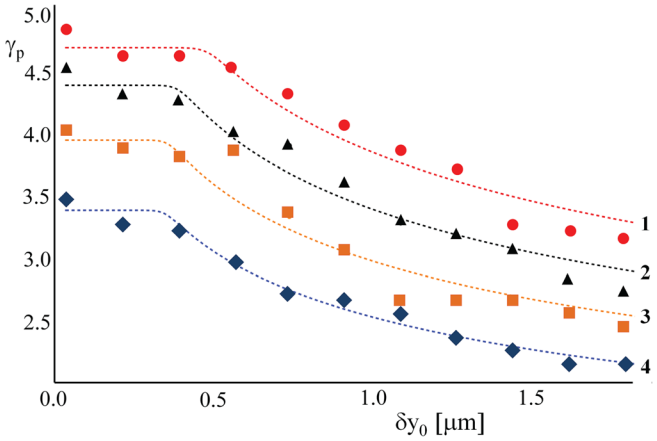

FIG. 7. The maximum normalized proton energy, $\gamma_p = \mathcal{E}_p/m_p$, gained with a mass limited target accelerated by a Gaussian laser pulse versus the initial off-axis displacement of the target for different dimensionless amplitudes: (1) $a = 325$, (2) $a = 300$, (3) $a = 275$, and (4) $a = 250$. The markers denote the simulation results, the curves correspond to an approximation by Eq. (58).

The dependence of the accelerated ion energy, $\mathcal{E}_\alpha$, on the initial transverse position of the target, $\delta r_0 = \delta y_0$, is presented in Fig. 7 for different laser pulse amplitudes. Under the simulation conditions, the accelerated ions reach their maximum energy at a time of approximately 250 fs; hence, all the graphs correspond to that moment of time. In Fig. 7, markers denote the normalized maximum energy of ions, γ_p, obtained in simulations for $a = 325$, 300, 275, and 250. The theoretical curves (denoted by dashed lines) are calculated as follows. The theoretical dependence of the ion energy on the initial target position follows from Eqs. (40) and (41):

$$\mathcal{E}_{\alpha,\delta r_0} = m_\alpha c^2 \frac{2^{1/2}}{3} \frac{l_\perp^{3/4}}{c^{1/2} t_{1/3}^{1/2} \delta r_0^{1/4}}. \tag{57}$$

This expression is valid for sufficiently large values of δr_0, provided that during the acceleration, the target does not move out of the path of the laser pulse. When $\delta r_0 \to 0$, the energy gain, Eq. (57), formally tends to infinity. Obviously, the ion energy from the off-axis localized target cannot be larger than the ion energy in the case of a target positioned exactly on the axis, $\mathcal{E}_{\alpha,max}$. To take this into account and fit the data in Fig. 7, we use the interpolation formula

$$\frac{1}{\mathcal{E}_\alpha^s} = \frac{1}{\mathcal{E}_{\alpha,max}^s} + \frac{1}{\mathcal{E}_{\alpha,\delta r_0}^s} \tag{58}$$

with a fit parameter, $s \gg 1$. According to this formula, in the limit of a small δr_0, the ion energy is equal to $\mathcal{E}_{\alpha,max}$. For a large initial vertical coordinate, it is asymptotically proportional to $\delta r_0^{-1/4}$, in accordance with Eq. (57).

According to Eq. (57), the ion energy decreases with increasing δr_0. In simulations, this decrease is slower than predicted by theory when the initial transverse shift of the target is sufficiently small, as shown in Fig. 7. This is due to self-modulation of the laser pulse in the transverse direction, which is distinctly seen in the electromagnetic field distribution in Fig. 4(b). The laser pulse self-modulation prevents the target from slippage out of the acceleration phase, thus elongating the acceleration and causing ion beam collimation, as seen in Fig. 6(e). As it follows from the dependences presented in Fig. 7, the laser pulse modulation effects are significant for $\delta y_0 < 0.5\mu$m.

IV. CONCLUSIONS AND DISCUSSION

We presented a study on the effects of the laser pulse transverse inhomogeneity on the radiation pressure-dominant acceleration of ions. Within the framework of a thin foil approximation, we found the dependence of the accelerated ion maximum energy on the off-axis displacement of a mass limited target for Gaussian and super-Gaussian laser pulse profiles. When the target was irradiated by the Gaussian laser pulse, it was pushed away from the pulse by the ponderomotive pressure of electromagnetic radiation, whereas in the case of a super-Gaussian pulse, the central part of the target could undergo self-contraction, provided its initial off-axis displacement was sufficiently small. The 2D PIC simulations corroborated the theoretical calculations if the target had a large initial coordinate in the vertical direction. If the target was positioned in the vicinity of the axis, the self-modulation of the laser pulse in the transverse direction prevented the target from slipping out of the acceleration phase, thereby elongating the acceleration and causing ion beam collimation.

The obtained results can be used to determine the required in experiment laser-target alignment parameters and/or as diagnostics for ion acceleration by the laser radiation pressure.

ACKNOWLEDGMENTS

Kirill Lezhnin was supported by Dynasty Foundation through the Scholarship Program for Students in Theoretical Physics.

[1]M. Borghesi, J. Fuchs, S. V. Bulanov, A. J. Mackinnon, P. Patel, and M. Roth, Fusion Sci. Technol. **49**, 412 (2006).
[2]A. V. Korzhimanov, A. A. Gonoskov, E. A. Khazanov, and A. M. Sergeev, Phys. Usp. **54**, 9 (2011).
[3]H. Daido, M. Nishiuchi, and A. S. Pirozhkov, Rep. Prog. Phys. **75**, 056401 (2012).
[4]A. Macchi, M. Passoni, and M. Borghesi, Rev. Mod. Phys. **85**, 751 (2013).
[5]S. Yu. Gus'kov, Plasma Phys. Rep. **39**, 1 (2013).
[6]S. V. Bulanov, J. J. Wilkens, M. Molls, T. Zh. Esirkepov, G. Korn, G. Kraft, S. D. Kraft, and V. S. Khoroshkov, Phys. Usp. **57**, 1149 (2014).
[7]S. V. Bulanov, T. Zh. Esirkepov, M. Kando, J. Koga, K. Kondo, and G. Korn, Plasma Phys. Rep. **41**, 1 (2015).
[8]V. S. Beskin, *MHD Flows in Compact Astrophysical Objects* (Springer, Berlin, 2010).
[9]E. V. Derishev, V. V. Kocharovsky, and Vl. V. Kocharovsky, Astrophys. J. **521**, 640 (1999).
[10]B. E. Stern and J. Poutanen, Mon. Not. R. Astron. Soc. **383**, 1695 (2008).
[11]D. Khangulyan, F. Aharonian, and V. Bosch-Ramon, Mon. Not. R. Astron. Soc. **383**, 467 (2008).
[12]B. Cerutti, A. Philippov, K. Parfrey, and A. Spitkovsky, Mon. Not. R. Astron. Soc. (in press) http://arxiv.org/abs/1410.3757.
[13]A. V. Gurevich, L. V. Pariskaya, and L. P. Pitaevskii, Sov. Phys. JETP **22**, 449 (1966).
[14]P. Mora, Phys. Rev. Lett. **90**, 185002 (2003).
[15]S. Wilks, W. L. Kruer, M. Tabak, and A. B. Langdon, Phys. Rev. Lett. **69**, 1383 (1992).
[16]S. P. Hatchett, C. G. Brown, T. E. Cowan, E. A. Henry, J. S. Johnson, M. H. Key, J. A. Koch, A. B. Langdon, B. F. Lasinski, R. W. Lee, A. J. Mackinnon, D. M. Pennington, M. D. Perry, T. W. Phillips, M. Roth, T. C.

Sangster, M. S. Singh, R. A. Snavely, M. A. Stoyer, S. C. Wilks, and K. Yasuike, Phys. Plasmas **7**, 2076 (2000).
[17]I. Last, I. Schek, and J. Jortner, J. Chem. Phys. **107**, 6685 (1997).
[18]K. Nishihara, H. Amitani, M. Murakami, S. V. Bulanov, and T. Zh. Esirkepov, Nucl. Instrum. Methods Phys. Res., Sect. A **464**, 98 (2001).
[19]V. F. Kovalev and V. Yu. Bychenkov, Phys. Rev. Lett. **90**, 185004 (2003).
[20]M. Murakami and M. M. Basko, Phys. Plasmas **13**, 012105 (2006).
[21]V. I. Veksler, At. Energy **2**, 525 (1957).
[22]T. Zh. Esirkepov, M. Borghesi, S. V. Bulanov, G. Mourou, and T. Tajima, Phys. Rev. Lett. **92**, 175003 (2004).
[23]O. Klimo, J. Psikal, J. Limpouch, and V. T. Tikhonchuk, Phys. Rev. Spec. Top. - Accel. Beams **11**, 031301 (2008).
[24]A. P. L. Robinson, M. Zepf, S. Kar, R. G. Evans, and C. Bellei, New J. Phys. **10**, 013021 (2008).
[25]V. A. Vshivkov, N. M. Naumova, F. Pegoraro, and S. V. Bulanov, Phys. Plasmas **5**, 2727 (1998).
[26]S. V. Bulanov, T. Zh. Esirkepov, M. Kando, S. S. Bulanov, S. G. Rykovanov, and F. Pegoraro, Phys. Plasmas **20**, 123114 (2013).
[27]A. Macchi, S. Veghini, and F. Pegoraro, Phys. Rev. Lett. **103**, 085003 (2009).
[28]S. S. Bulanov, C. B. Schroeder, E. Esarey, and W. P. Leemans, Phys. Plasmas **19**, 093112 (2012).
[29]S. Kar, M. Borghesi, S. V. Bulanov, A. Macchi, M. H. Key, T. V. Liseykina, A. J. Mackinnon, P. K. Patel, L. Romagnani, A. Schiavi, and O. Willi, Phys. Rev. Lett. **100**, 225004 (2008).
[30]A. Henig, S. Steinke, M. Schnuerer, T. Sokollik, R. Hoerlein, D. Kiefer, D. Jung, J. Schreiber, B. M. Hegelich, X. Q. Yan, J. Meyer-ter-Vehn, T. Tajima, P. V. Nickles, W. Sandner, and D. Habs, Phys. Rev. Lett. **103**, 245003 (2009).
[31]S. Kar, K. F. Kakolee, B. Qiao, A. Macchi, M. Cerchez, D. Doria, M. Geissler, P. McKenna, D. Neely, J. Osterholz, R. Prasad, K. Quinn, B. Ramakrishna, G. Sarri, O. Willi, X. Y. Yuan, M. Zepf, and M. Borghesi, Phys. Rev. Lett. **109**, 185006 (2012).
[32]J. Limpouch, J. Psikal, A. A. Andreev, K. Yu. Platonov, and S. Kawata, Laser Part. Beams **26**, 225 (2008).
[33]A. A. Andreev, J. Limpouch, J. Psikal, K. Yu. Platonov, and V. T. Tikhonchuk, Eur. Phys. J.: Spec. Top. **175**, 123 (2009).
[34]T. Kluge, W. Enghardt, S. D. Kraft, U. Schramm, K. Zeil, T. E. Cowan, and M. Bussmann, Phys. Plasmas **17**, 123103 (2010).
[35]K. Zeil, J. Metzkes, T. Kluge, M. Bussmann, T. E. Cowan, S. D. Kraft, R. Sauerbrey, B. Schmidt, M. Zier, and U. Schramm, Plasma Phys. Controlled Fusion **56**, 084004 (2014).
[36]A. Zigler, S. Eisenman, M. Botton, E. Nahum, E. Schleifer, A. Baspaly, I. Pomerantz, F. Abicht, J. Branzel, G. Priebe, S. Steinke, A. Andreev, M. Schnuerer, W. Sandner, D. Gordon, P. Sprangle, and K. W. D. Ledingham, Phys. Rev. Lett. **110**, 215004 (2013).
[37]J. W. Wang, M. Murakami, S. M. Weng, H. Xu, J. J. Ju, S. X. Luan, and W. Yu, Phys. Plasmas **21**, 123103 (2014).
[38]T. P. Yu, Z. M. Sheng, Y. Yin, H. B. Zhuo, Y. Y. Ma, F. Q. Shao, and A. Pukhov, Phys. Plasmas **21**, 053105 (2014).
[39]Y. Fukuda, A. Ya. Faenov, M. Tampo, T. A. Pikuz, T. Nakamura, M. Kando, Y. Hayashi, A. Yogo, H. Sakaki, T. Kameshima, A. S. Pirozhkov, K. Ogura, M. Mori, T. Zh. Esirkepov, J. Koga, A. S. Boldarev, V. A. Gasilov, A. I. Magunov, T. Yamauchi, R. Kodama, P. R. Bolton, Y. Kato, T. Tajima, H. Daido, and S. V. Bulanov, Phys. Rev. Lett. **103**, 165002 (2009).
[40]S. V. Bulanov, T. Zh. Esirkepov, M. Kando, A. S. Pirozhkov, and N. N. Rosanov, Phys. Usp. **56**, 429 (2013).
[41]T.-P. Yu, A. M. Pukhov, Z.-M. Sheng, F. Liu, and G. Shvets, Phys. Rev. Lett. **110**, 045001 (2013).
[42]S. V. Bulanov, E. Yu. Echkina, T. Zh. Esirkepov, I. N. Inovenkov, M. Kando, F. Pegoraro, and G. Korn, Phys. Rev. Lett. **104**, 135003 (2010).
[43]S. V. Bulanov, E. Yu. Echkina, T. Zh. Esirkepov, I. N. Inovenkov, M. Kando, F. Pegoraro, and G. Korn, Phys. Plasmas **17**, 063102 (2010).
[44]F. Pegoraro and S. V. Bulanov, Phys. Rev. Lett. **99**, 065002 (2007).
[45]E. Yu. Echkina, I. N. Inovenkov, T. Zh. Esirkepov, F. Pegoraro, M. Borghesi, and S. V. Bulanov, Plasma Phys. Rep. **36**, 15 (2010).
[46]T. Zh. Esirkepov, Comput. Phys. Commun. **135**, 144 (2001).
[47]E. Ott, Phys. Rev. Lett. **29**, 1429 (1972).
[48]W. Manheimer, D. Colombait, and E. Ott, Phys. Fluids **27**, 2164 (1984).
[49]T. Taguchi and K. Mima, Phys. Plasmas **2**, 2790 (1995).
[50]G. A. Korn and T. M. Korn, *Mathematical Handbook for Scientists and Engineers* (Dover Publication, New York, 2000).
[51]S. V. Bulanov, T. Zh. Esirkepov, M. Kando, F. Pegoraro, S. S. Bulanov, C. G. R. Geddes, C. B. Schroeder, E. Esarey, and W. P. Leemans, Phys. Plasmas **19**, 103105 (2012).
[52]S. S. Bulanov, E. Esarey, C. B. Schroeder, S. V. Bulanov, T. Zh. Esirkepov, M. Kando, F. Pegoraro, and W. P. Leemans, Phys. Rev. Lett. (in press).
[53]S. Humphries, Jr., *Principles of Charged Particle Acceleration* (Wiley, New York, 1999).
[54]A. Zhidkov, J. Koga, A. Sasaki, and M. Uesaka, Phys. Rev. Lett. **88**, 185002 (2002).
[55]S. V. Bulanov, T. Zh. Esirkepov, J. Koga, and T. Tajima, Plasma Phys. Rep. **30**, 196 (2004).
[56]M. Tamburini, T. V. Liseykina, F. Pegoraro, and A. Macchi, Phys. Rev. E **85**, 016407 (2012).
[57]S. S. Bulanov, C. B. Schroeder, E. Esarey, and W. P. Leemans, Phys. Rev. A **87**, 062110 (2013).
[58]T. Zh. Esirkepov, S. S. Bulanov, J. K. Koga, M. Kando, K. Kondo, N. N. Rosanov, G. Korn, and S. V. Bulanov, e-print arXiv:1412.6028v1 [physics.plasm-ph](2014).